IEEE Access
Multidisciplinary ⋮ Rapid Review ⋮ Open Access Journal

Date of publication xxxx 00, 0000, date of current version xxxx 00, 0000.

Digital Object Identifier 10.1109/ACCESS.2017.Doi Number

Volume Conservation Constrained Multi-Material Reconstruction for Inconsistent Spectral CT Imaging

Xiaohuan Yu[1], Ailong Cai[1], Ningning Liang[1], Shaoyu Wang[1], Lei Li[1], Bin Yan[1]

[1] Henan Key Laboratory of Imaging and Intelligent Processing, PLA Strategic Support Force Information Engineering University, Zhengzhou, China

Corresponding author: Bin Yan (e-mail: ybspace@hotmail.com).

This work was supported by the National Natural Science Foundation of China under Grant 62101596 and Grant 62201616. This work was also supported by the National Key Research and Development Project of China under Grant 2020YFC1522002 and the China Postdoctoral Science Foundation under Grant 2019M663996.

ABSTRACT Spectral computed tomography (spectral CT) is a promising medical imaging technology because of its ability to provide information on material characterization and quantification. However, the difficulty of decomposition also increases due to the nonlinearity nature of the measurements and ill condition of the problem, especially in the case of geometric inconsistency, which typically leads to low image qualities. Therefore, it is a crucial issue for inconsistent spectral CT imaging to improve the accuracy of material decomposition while suppressing the noise. This paper depends on a statistical reconstruction model with different priors to propose one-step multi-material algorithms. In these approaches, the gradient sparisty-based and convolutional neural network based methods are designed for the case of the consistent numbers of material and energies. And volume conservation constraint are further developed while the two numbers are not equal. An efficient Newton descent method is adopted based on the simple surrogate function. For simulation experiments with different noise levels, the largest peak signal-to-noise ratio (PSNR) obtained by the proposed method approximately increases by 20.924 dB and 18.283 dB compared with those of other algorithms. Magnified areas of real data also further demonstrated that the proposed methods has a better ability to suppress noise. Numerical experiments verify that the proposed method efficiently reconstructed the material maps, and reduced noise compared with the state-of-the-art methods.

INDEX TERMS Spectral computed tomography, Image reconstruction, One-step material decomposition, Inconsistent geometry.

I. INTRODUCTION

Spectral computed tomography (spectral CT) has promising potentials in wide applications due to its ability of quantitative material discrimination for diagnostics and therapy evaluation in medical imaging[1-3]. Evidences are becoming found indicating that spectral CT can help to improve the diagnosis of coronavirus disease (COVID-19)[4, 5]. As one of the typical implementations of spectral CT, the principle of dual-energy CT (DECT) has been studied for a long time. Recent developments of energy selective detectors have spurred the research in this area, especially the improvement of photon-counting detectors (PCDs)[6]. However, the low signal-to-noise ratio (SNR) measurements, caused by pile-up, fluorescence effect, charge sharing, and photon scattering, affects the image quality as well as the accuracy of material decomposition[7]. In the process of imaging, quantum noise, electronic noise and reconstruction noise introduced by hardware devices and algorithms will degrade our imaging results. As well as the development of equipment, optimizing algorithms and parameters are critical in the field of medical imaging to improve the accuracy of material decomposition and maintain image quality.

In recent years, there are two categories of methods to reconstruct the material-specific images: two-step methods and one-step methods. Furthermore, the two-step methods can be divided into image-domain and projection-domain based methods. The image-domain based approaches[8-11] firstly reconstruct CT images from the polychromatic projection data, and then obtain the corresponding material images by a decomposition step on CT images. Unfortunately, the quality of material results is always severely affected by beam hardening artifact and noise explosion caused by direct matrix inversion-based decomposition, especially when there are more than two materials to be separated[12]. On the other hand, for projection-domain based methods, the multi-energy projections are first separated or decomposed into material-specific projections, and then reconstructed through conventional algorithms[13-15]. However, it requires the projection in multi-energy measured under strictly consistent and identical imaging geometry (i.e., the same source, object and detector positions), which limits its application in fast kVp switching[16] or multi-source-multi-detector[17] systems. In addition, the material-specific results of two-step methods is dependent on the quality of the first step, and it is difficult for the second step to compensate for the errors caused by the first step.

To avoid these problems for dual material imaging in dual spectral CT, several methods aiming at directly obtaining material-specific images from the nonlinear observation measurements have been proposed, called one-step iterative methods above mentioned, which typically combines forward models of the reconstruction with the material separation process. For instance, Zhao et al. utilized the first-order Taylor expansion of nonlinear observations and proposed an extended algebraic reconstruction technique (EART)[18] for DECT. For the consideration of the convergence efficiency, a couple variants of EART have been proposed in recent years, e.g., the simultaneous EART (ESART)[19], the monochromatic images guided iteration method[20] for dual-energy, which accelerates the convergence but needs to manually determine the optimal values of reference energy. And the oblique projection modification technique (OPMT)[21] for the inconsistent scanning to acquire the material-specific maps. In addition, since the photons emitted by X-ray source often contain some statistical significance, different statistical iterative methods have emerged. Xu et al.[22] developed a penalized-likelihood algorithm to implement the basis materials decomposition for DECT. Long et al.[23], Weidinger et al.[24] and Mechlem et al.[25] designed the separable quadratic surrogates of spectral CT statistical models to achieve the one-step material decompositions. Barber et al.[26] applied the primal-dual prototyping framework to material imaging of spectral CT. Very recently, they further proposed to investigate the convergence theory of the nonconvex alternating direction of multipliers method (NcADMM)[27] and conducted the reconstruction of PCD system for the purpose of reducing beam-hardening and metal artifacts[28]. It is more difficult to solve the inverse problem when the occasion comes into inconsistent scanning system.

Moreover, since the CT inverse problem is always ill-conditioned, it is often necessary to incorporate prior knowledge as regularization term to suppress the noise of basis material images. Some sparsity-based methods are applied to improve the reconstruction quality. For example, Cai et al.[29] adopted Huber function[30] as the regularization term in a Bayesian approach. Chen et al.[31, 32] applied the convex indicator function of the gradient image to enforce an upper bound on the material images and monochromatic images. Zhang et al.[33] proposed a direct material reconstruction method that combined total variation (TV) and block-matching and 3D filtering for DECT. However, for the above one-step iterative method, some methods are even susceptible to noise due to lack the ability of noise suppression or one need to adjust the parameters of the regularization terms manually when the number of materials increases. Direct extensions and applications of the above-mentioned one-step methods to multi-material reconstructions are unstable or will even cause failure, due to the increase of the ill-posedness for the case of inconsistent geometry. Therefore, it is a key issue to design an efficient and accurate one-step method based on an appropriate optimization model for multi-material imaging in spectral CT.

In this work, for multi-material reconstruction under inconsistent geometry, a statistical reconstruction model is established combining different material-specific image regularization priors. For the case where the number of spectrums matches the number of materials, a gradient sparsity TV based prior and a convolutional neural network, denoising convolutional neural network (DnCNN)[34], based prior are incorporated into the statistical model. For the case where the number of spectrums does not match the number of materials, a new volume conservation constraint (VCC) is developed to improve the ill condition of the inverse problem. Moreover, an efficient Newton descent algorithm based on the simple

surrogate function. To verify the practical performance of the presented method, a series of numerical experiments have been conducted and shown that the proposed algorithms have an improved results of noise suppression compared with the state-of-the-art one-step material reconstruction methods.

The organization of this paper is as follow. Section 2 introduces the physical model, and describe the proposed reconstruction algorithms. Section 3 presents the numerical verifications of the proposed method and experimental comparisons with typical competing methods. Discussions and conclusions are subsequently presented in Section 4 and Section 5, respectively.

II. MATERIALS AND METHODS

A. STATISTICAL MULTI-MATERIAL RECONSTRUCTION MODEL

Spectral computed tomography (spectral CT) utilizes the attenuation differences of different materials when passing the polychromatic X-ray. The attenuation of object $\boldsymbol{f}(x,E)$ at ray l under spectrum $S_s(E)$ follows the formula:

$$y_{s,l}=\int S_s(E)\exp(-\int_l \boldsymbol{f}(x,E)dl)dE, \tag{1}$$

where $l\in\Omega_s, s=1,2,...,S$. Further, $\boldsymbol{f}(x,E)$ can be decoupled into a linear combination of energy-dependent term $\mu_k(E)$ and basis material-dependent term $\boldsymbol{f}_k(x)$, i.e.,

$$\boldsymbol{f}(x,E)=\sum_{k=1}^{K}\mu_k(E)\,\boldsymbol{f}_k(x), \tag{2}$$

where K is the total number of basis materials. In general, the discrete form is utilized to establish the transmission model:

$$y_{s,l}=\sum_{m=1}^{M_s}S_{s,m}\exp(-\sum_{k=1}^{K}\mu_{m,k}A_{s,l}\boldsymbol{f}_k), \tag{3}$$

where $S_{s,m}$ is the sampling point of the energy spectrum $S_s(E)$, and $\sum_{m=1}^{M_s}S_{s,m}=1$. $A_{s,l}$ represents the line integral of basis material $\boldsymbol{f}_k$ and the path of the ray l. For the photon counting detector, the measurements is assumed to follow the Poisson model:

$$y_{s,l}\sim Poisson(\sum_{m=1}^{M_s}S_{s,m}\exp(-\sum_{k=1}^{K}\mu_{m,k}A_{s,l}\boldsymbol{f}_k)), \tag{4}$$

For the inconsistent scanning geometry, the path of the measured ray under one spectrum do not coincide another spectrum. In other words, the intersection of any two sets of ray l is empty ($\Omega_{s1}\cap\Omega_{s2}=\varnothing,\ s1,s2\in\{1,...,S\}$). Assuming that the measured photons $y_{s,l}$ follow Poisson statistical model. Given the measurements $\hat{y}$, the negative log-likelihood function with respect to the photons is

$$L(\boldsymbol{f}_1,\boldsymbol{f}_2,\cdots\boldsymbol{f}_K)=\sum_{s,l}y_{s,l}(\boldsymbol{f}_1,\boldsymbol{f}_2,\cdots\boldsymbol{f}_K)-\hat{y}_{s,l}\ln y_{s,l}(\boldsymbol{f}_1,\boldsymbol{f}_2,\cdots\boldsymbol{f}_K). \tag{5}$$

However, minimizing the negative log-likelihood function for the polychromatic measurements is always ill-posed due to the severe noise. It is need to combine with some prior knowledge as regularization term to improve the condition of solution. Therefore, the multi-material reconstruction model is descripted as

$$\min_{\boldsymbol{f}_1,\boldsymbol{f}_2,\cdots\boldsymbol{f}_K}L(\boldsymbol{f}_1,\boldsymbol{f}_2,\cdots\boldsymbol{f}_K)+\lambda R(\boldsymbol{f}_1,\boldsymbol{f}_2,\cdots\boldsymbol{f}_K) \tag{6}$$

where $R(\boldsymbol{f}_1,\boldsymbol{f}_2,\cdots\boldsymbol{f}_K)$ is the mathematical symbolic representation of prior knowledge, such as gradient sparsity of reconstructed images and other material-specific knowledge. λ is a scaling nonnegative factor to balance the regularization term.

B. PRIORS BASED METHODS FOR INCONSISTENT POLYCHROMATIC PROJECTION

From the definition of $L(\boldsymbol{f}_1,\boldsymbol{f}_2,\cdots\boldsymbol{f}_K)$, there is the operations of summing first and then taking logarithm, it is difficult to obtain the analytical solution directly. One intuitive idea is to find a simple representation of the complex function that is easier to solve. Before the final representation obtained, we first rewrite the equation (5) as

$$\begin{aligned}&L(\boldsymbol{f}_1,\boldsymbol{f}_2,\cdots\boldsymbol{f}_K)=\sum_{s,l}y_{s,l}(\boldsymbol{f}_1,\boldsymbol{f}_2,\cdots\boldsymbol{f}_K)-\hat{y}_{s,l}\ln y_{s,l}(\boldsymbol{f}_1,\boldsymbol{f}_2,\cdots\boldsymbol{f}_K)\\&=\sum_{s,l}\sum_{m=1}^{M_s}S_{s,m}\exp(-\sum_{k=1}^{K}\mu_{m,k}A_{s,l}\boldsymbol{f}_k)-\hat{y}_{s,l}\ln\sum_{m=1}^{M_s}S_{s,m}\exp(-\sum_{k=1}^{K}\mu_{m,k}A_{s,l}\boldsymbol{f}_k)\\&=\sum_{s,l}\sum_{m=1}^{M_s}\frac{S_{s,m}}{\alpha^{(n)}}\alpha^{(n)}t(\boldsymbol{f}_1,\boldsymbol{f}_2,\cdots\boldsymbol{f}_K)-\hat{y}_{s,l}\ln\sum_{m=1}^{M_s}\frac{S_{s,m}}{\alpha^{(n)}}\alpha^{(n)}t(\boldsymbol{f}_1,\boldsymbol{f}_2,\cdots\boldsymbol{f}_K),\end{aligned} \tag{7}$$

where $t(\boldsymbol{f}_1,\boldsymbol{f}_2,\cdots\boldsymbol{f}_K)=\exp(-\sum_{k=1}^{K}\mu_{m,k}A_{s,l}\boldsymbol{f}_k)$, and $\alpha^{(n)}$ is a nonnegative parameter. To get a more explicit expression of parameter $\alpha^{(n)}$, it is necessary to state that $\alpha^{(n)}$ satisfies the assumption $\sum_{m=1}^{M_s}\alpha^{(n)}=\sum_{m=1}^{M_s}\alpha(\boldsymbol{f}_1^{(n)},...,\boldsymbol{f}_K^{(n)})=1$. Combining with the fact that $h(x)=x-y\ln x$ is a convex function, the above equation (7) transformed into finding its upper bound by Jensen's inequality

$$\begin{aligned}&L(\boldsymbol{f}_1,\boldsymbol{f}_2,\cdots\boldsymbol{f}_K)\\&=\sum_{s,l}\sum_{m=1}^{M_s}\frac{S_{s,m}}{\alpha^{(n)}}\alpha^{(n)}t(\boldsymbol{f}_1,\boldsymbol{f}_2,\cdots\boldsymbol{f}_K)-\hat{y}_{s,l}\ln\sum_{m=1}^{M_s}\frac{S_{s,m}}{\alpha^{(n)}}\alpha^{(n)}t(\boldsymbol{f}_1,\boldsymbol{f}_2,\cdots\boldsymbol{f}_K)\\&\le\sum_{s,l}\sum_{m=1}^{M_s}\alpha^{(n)}[\frac{S_{s,m}}{\alpha^{(n)}}t(\boldsymbol{f}_1,\boldsymbol{f}_2,\cdots\boldsymbol{f}_K)-\hat{y}_{s,l}\ln\frac{S_{s,m}}{\alpha^{(n)}}t(\boldsymbol{f}_1,\boldsymbol{f}_2,\cdots\boldsymbol{f}_K)].\end{aligned} \tag{8}$$

If the equality holds, the upper bound close to the original objective function $L(\boldsymbol{f}_1,\boldsymbol{f}_2,\cdots\boldsymbol{f}_K)$. Therefore, we need to construct a proper $\alpha^{(n)}$ to make the equality holds, i.e., the equality holds if and only if the value is a constant. Hence, the following equation at point $(\boldsymbol{f}_1^{(n)},...,\boldsymbol{f}_K^{(n)})$ is established

$$\frac{S_{s,m}}{\alpha^{(n)}}t(\boldsymbol{f}_1^{(n)},...,\boldsymbol{f}_K^{(n)})=c, \tag{9}$$

where c is a constant. According to $\sum_{m=1}^{M_s}\alpha^{(n)}=1$, we get the explicit formula of $\alpha^{(n)}$ as

$$\alpha^{(n)}=\frac{S_{s,m}t(\boldsymbol{f}_1^{(n)},...,\boldsymbol{f}_K^{(n)})}{\sum_{m=1}^{M_s}S_{s,m}t(\boldsymbol{f}_1^{(n)},...,\boldsymbol{f}_K^{(n)})}=\frac{S_{s,m}t^{(n)}}{\sum_{m=1}^{M_s}S_{s,m}t^{(n)}}=\frac{S_{s,m}t^{(n)}}{y_{s,l}^{(n)}}. \tag{10}$$

We further denote $\beta^{(n)}=\frac{S_{s,m}}{\alpha^{(n)}}=\frac{y_{s,l}^{(n)}}{t^{(n)}}$, then $\alpha^{(n)}=\frac{S_{s,m}}{\beta^{(n)}}$ and

$$\begin{aligned}
&L(\boldsymbol{f}_1,\boldsymbol{f}_2,\cdots\boldsymbol{f}_K)\\
&\le\sum_{s,l}\sum_{m=1}^{M_s}\alpha^{(n)}[\frac{S_{s,m}}{\alpha^{(n)}}t(\boldsymbol{f}_1,\boldsymbol{f}_2,\cdots\boldsymbol{f}_K)-\hat{y}_{s,l}\ln\frac{S_{s,m}}{\alpha^{(n)}}t(\boldsymbol{f}_1,\boldsymbol{f}_2,\cdots\boldsymbol{f}_K)]\\
&=\sum_{s,l}\sum_{m=1}^{M_s}\frac{S_{s,m}}{\beta^{(n)}}(\beta^{(n)}t(\boldsymbol{f}_1,\boldsymbol{f}_2,\cdots\boldsymbol{f}_K)-\hat{y}_{s,l}\ln\beta^{(n)}t(\boldsymbol{f}_1,\boldsymbol{f}_2,\cdots\boldsymbol{f}_K)) \qquad (11)\\
&=\sum_{m=1}^{M_s}S_{s,m}\sum_{s,l}\frac{1}{\beta^{(n)}}(\beta^{(n)}t(\boldsymbol{f}_1,\boldsymbol{f}_2,\cdots\boldsymbol{f}_K)-\hat{y}_{s,l}\ln\beta^{(n)}t(\boldsymbol{f}_1,\boldsymbol{f}_2,\cdots\boldsymbol{f}_K))\\
&=\sum_{m=1}^{M_s}S_{s,m}\hat{L}(\boldsymbol{f}_1,\boldsymbol{f}_2,\cdots\boldsymbol{f}_K),
\end{aligned}$$

where

$$\hat{L}(\boldsymbol{f}_1,\boldsymbol{f}_2,\cdots\boldsymbol{f}_K)=\sum_{s,l}\frac{1}{\beta^{(n)}}(\beta^{(n)}t(\boldsymbol{f}_1,\boldsymbol{f}_2,\cdots\boldsymbol{f}_K)-\hat{y}_{s,l}\ln\beta^{(n)}t(\boldsymbol{f}_1,\boldsymbol{f}_2,\cdots\boldsymbol{f}_K)).$$

And $\sum_{m=1}^{M_s}S_{s,m}\hat{L}(\boldsymbol{f}_1,\boldsymbol{f}_2,\cdots\boldsymbol{f}_K)$ is the desired final representation mentioned at the beginning of the subsection. Although the original objective function $L(\boldsymbol{f}_1,\boldsymbol{f}_2,\cdots\boldsymbol{f}_K)$ is approximated, the simple function is equivalent to $L(\boldsymbol{f}_1,\boldsymbol{f}_2,\cdots\boldsymbol{f}_K)$ at a certain point from the construction process.

C. GRADIENT SPARSITY-BASED ALGORITHM

In this subsection, the total variation (TV) is utilized to characterize the material maps sparsity, i.e., the regularization term $R(\boldsymbol{f}_1,\boldsymbol{f}_2,\cdots\boldsymbol{f}_K)=\sum_{k=1}^{K}\|\nabla\boldsymbol{f}_k\|_1$, where $\nabla\boldsymbol{f}_k:=(\nabla_x\boldsymbol{f}_k,\nabla_y\boldsymbol{f}_k)$ denotes differential operator along the x and y directions. And the TV term is defined as

$$\|\nabla\boldsymbol{f}_k\|_1=\|\nabla_x\boldsymbol{f}_k\|_1+\|\nabla_y\boldsymbol{f}_k\|_1. \tag{12}$$

Therefore, the gradient sparsity based reconstruction model can be illustrate as

$$\min_{\boldsymbol{f}_1,\boldsymbol{f}_2,\cdots\boldsymbol{f}_K}\sum_{m=1}^{M_s}S_{s,m}\hat{L}(\boldsymbol{f}_1,\boldsymbol{f}_2,\cdots\boldsymbol{f}_K)+\lambda\sum_{k=1}^{K}\|\nabla\boldsymbol{f}_k\|_1 \tag{13}$$

To solve the optimization problem, the Newton method is applied to get new iterations in the following equation

$$\begin{aligned}
\boldsymbol{f}_k^{(n+1)}&=\boldsymbol{f}_k^{(n)}-\Delta\boldsymbol{f}_k^{(n)}\\
&=\boldsymbol{f}_k^{(n)}-\sum_k\frac{(\sum_{m=1}^{M_k}S_{s,m}\frac{\partial\hat{L}(\boldsymbol{f}_1,\boldsymbol{f}_2,\cdots\boldsymbol{f}_K)}{\boldsymbol{f}_k}+\lambda\frac{\partial\sum_{k=1}^{K}\|\nabla\boldsymbol{f}_k\|_1}{\boldsymbol{f}_k})\Big|_{\boldsymbol{f}_k=\boldsymbol{f}_k^{(n)}}}{(\frac{\partial^2\hat{L}(\boldsymbol{f}_1,\boldsymbol{f}_2,\cdots\boldsymbol{f}_K)}{\partial\boldsymbol{f}_k^{\,2}}+\frac{\partial^2\sum_{k=1}^{K}\|\nabla\boldsymbol{f}_k\|_1}{\partial\boldsymbol{f}_k^{\,2}})\Big|_{\boldsymbol{f}_k=\boldsymbol{f}_k^{(n)}}}\\
&=\boldsymbol{f}_k^{(n)}-\sum_k\frac{\sum_{s,l}A_{s,l}^T\cdot(\frac{\hat{y}_{s,l}}{y_{s,l}^{(n)}}-1)\sum_{m=1}^{M_k}S_{s,m}\mu_{m,k}t^{(n)}+\lambda\nabla^T\|\nabla\boldsymbol{f}_k\|_1\Big|_{\boldsymbol{f}_k=\boldsymbol{f}_k^{(n)}}}{\sum_{s,l}A_{s,l}^T\cdot A_{s,l}\cdot\sum_{m=1}^{M_k}S_{s,m}\mu_{m,k}^2t^{(n)}+diag(\nabla^T\nabla)},
\end{aligned}$$

$(k=1,2,...,K),$ (14)

where $diag(x)$ denotes the diagonal matrix of x. Note that the continuous function $\|\cdot\|_1$ is not differentiable, but for a discrete digital two-dimensional image, the symbols of the first and second derivatives here represent operations pixel-wised. The overall description of gradient sparsity-based method is summarized in Algorithm 1.

Algorithm 1. TV-based method

Input: measured projection data $\hat{y}_{s,l}$, parameter $\lambda, n_{\max}$.

Initialization: $\boldsymbol{f}_k^{(0)}(k=1,2,...,K)$, $n=0$.

While $n\le n_{\max}$

Update $\boldsymbol{f}_k^{(n)}(k=1,2,...,K)$ via (14).

End while

Output: $\boldsymbol{f}_k,(k=1,...,K)$

D. DEEP PRIOR-BASED ALGORITHM

Rather than the TV penalty, we also consider a deep prior, DnCNN, as a flexible module under the plug-and-play (PnP) framework[35]. The deep prior-based multi-material reconstruction model is

$$\min_{\boldsymbol{f}_1,\boldsymbol{f}_2,\cdots\boldsymbol{f}_K}\sum_{m=1}^{M_s}S_{s,m}\hat{L}(\boldsymbol{f}_1,\boldsymbol{f}_2,\cdots\boldsymbol{f}_K)+\lambda\sum_{k=1}^{K}\Phi(\boldsymbol{f}_k) \tag{15}$$

where $\Phi(\boldsymbol{f}_k)$ is the DnCNN deep prior in terms of k-th basis materials. Furthermore, auxiliary variables $\boldsymbol{g}_1,\boldsymbol{g}_2,\cdots\boldsymbol{g}_K$ are introduced to transform the problem as

$$\min_{\boldsymbol{f}_k,\boldsymbol{g}_k}\sum_{m=1}^{M_s}S_{s,m}\hat{L}(\boldsymbol{f}_1,\boldsymbol{f}_2,\cdots\boldsymbol{f}_K)+\lambda\sum_{k=1}^{K}\Phi(\boldsymbol{g}_k)+\sum_{k=1}^{K}\frac{\lambda_k}{2}\left\|\boldsymbol{f}_k-\boldsymbol{g}_k+\frac{\Lambda_k}{\lambda_k}\right\|_2^2,$$
$$k=1,...,K, \tag{16}$$

where Λ_k is the Lagrangian multiplier, and λ_k is the nonnegative penalty parameter. The alternating directions method of multipliers (ADMM) is adopted to solve problem (16), it is divided into two sub-problems

$$\begin{aligned}
\boldsymbol{f}_k^{(n+1)}&=\arg\min_{\boldsymbol{f}_k}\sum_{m=1}^{M_s}S_{s,m}\hat{L}(\boldsymbol{f}_1,\boldsymbol{f}_2,\cdots\boldsymbol{f}_K)+\sum_{k=1}^{K}\frac{\lambda_k}{2}\left\|\boldsymbol{f}_k-\boldsymbol{g}_k^{(n)}+\frac{\Lambda_k^{(n)}}{\lambda_k}\right\|_2^2\\
&=\boldsymbol{f}_k^{(n)}-\sum_k\frac{\sum_{s,l}A_{s,l}^T\cdot(\frac{\hat{y}_{s,l}}{y_{s,l}^{(n)}}-1)\sum_{m=1}^{M_k}S_{s,m}\mu_{m,k}t^{(n)}+\lambda_k(\boldsymbol{f}_k-\boldsymbol{g}_k^{(n)}+\frac{\Lambda_k^{(n)}}{\lambda_k})\Big|_{\boldsymbol{f}_k=\boldsymbol{f}_k^{(n)}}}{\sum_{s,l}A_{s,l}^T\cdot A_{s,l}\cdot\sum_{m=1}^{M_k}S_{s,m}\mu_{m,k}^2t^{(n)}+\lambda_k},
\end{aligned}$$
$$k=1,...,K, \tag{17}$$

$$\begin{aligned}
\boldsymbol{g}_k^{(n+1)}&=\arg\min_{\boldsymbol{g}_k}\sum_{k=1}^{K}\Phi(\boldsymbol{g}_k)+\sum_{k=1}^{K}\frac{1}{2\lambda_k/\lambda_k}\left\|\boldsymbol{f}_k^{(n+1)}-\boldsymbol{g}_k+\frac{\Lambda_k^{(n)}}{\lambda_k}\right\|_2^2\\
&=DnCNN(\boldsymbol{f}_k^{(n+1)}+\frac{\Lambda_k^{(n)}}{\lambda_k},\sqrt{\lambda_k/\lambda_k}),\ k=1,...,K.
\end{aligned} \tag{18}$$

In the implementation of sub-problem $\boldsymbol{g}_1,\boldsymbol{g}_2,\cdots\boldsymbol{g}_K$, it is a denoising process based on a pre-trained DnCNN network.

Feeding $\boldsymbol{f}_k^{(n+1)} + \frac{\Lambda_k^{(n)}}{\lambda_k}$ into the denoiser DnCNN network, we obtain the solution $\boldsymbol{g}_k^{(n+1)}$. The parameter $\sqrt{\lambda/\lambda_k}$ is related to the error estimation between the clean and noisy images. The summary of deep prior-based material reconstruction (DnCNN-based) method is listed in Algorithm 2.

Algorithm 2. DnCNN-based method

Input: measured projection data $\hat{y}_{s,l}$, parameter $\lambda, n_{\max}, \lambda_k (k = 1,...,K)$.

Initialization: $\boldsymbol{f}_k^{(0)}, \boldsymbol{g}_k^{(0)} (k = 1,2,...,K)$, $n = 0$.

While $n \le n_{\max}$

For $k = 1,2,...,K$

1. Update $\boldsymbol{f}_k^{(n)}$ via (17).
2. Update $\boldsymbol{g}_k^{(n)}$ via (18).
3. $\Lambda_k^{(n+1)} = \Lambda_k^{(n)} + \lambda_k (\boldsymbol{f}_k^{(n+1)} - \boldsymbol{g}_k^{(n+1)})$.

End while

Output: $\boldsymbol{f}_k, (k = 1,...,K)$

E. VOLUME CONSERVATION CONSTRATINT-BASED ALGORITHM

If the numbers of the basis material and spectrums are not same, i.e., the known spectrums is less than the number material, the nonlinear inverse problem can be described as

$$\begin{cases} y_{1,l} = \sum_{m=1}^{M_1} S_{1,m} \exp(-\sum_{k=1}^{K} \mu_{m,k} A_{1,l} \boldsymbol{f}_k), \\ y_{2,l} = \sum_{m=1}^{M_2} S_{1,m} \exp(-\sum_{k=1}^{K} \mu_{m,k} A_{2,l} \boldsymbol{f}_k), \\ \cdots \\ y_{s-1,l} = \sum_{m=1}^{M_{s-1}} S_{s-1,m} \exp(-\sum_{k=1}^{K} \mu_{m,k} A_{s-1,l} \boldsymbol{f}_k). \end{cases}$$

It means that the nonlinear equation system about the unknown basis materials $\boldsymbol{f}_k, k = 1,2,...,K$ is more ill-posed and the existence of noise will aggravate the difficulty of solving problem. Similar to the previous two subsections, the intuitive idea is to introduce regularization terms to suppress the adverse effects of noise. In addition, we further assume that the volume of basis materials in a voxel or pixel is conserved. Under this assumption, the volume conservation constraint is proposed for the first time to reduce the difficulty through adding nonlinear equations, which formulation is derived as (20). Therefore, the minimization is reformulated as

$$\min_{\boldsymbol{f}_1, \boldsymbol{f}_2, \cdots \boldsymbol{f}_K} \sum_{m=1}^{M_s} S_{s,m} \hat{L}(\boldsymbol{f}_1, \boldsymbol{f}_2, \cdots \boldsymbol{f}_K) + \lambda \sum_{k=1}^{K} \|\nabla \boldsymbol{f}_k\|_1 \quad s.t. \quad \sum_{k=1}^{K} \boldsymbol{f}_k = T_0, \quad (19)$$

where T_0 is a template and its pixel is 1 when the materials is present. We try to integrate this equality constraint in the descent step of basis materials. First, we convert the constraint into projection data at an auxiliary normalized spectrum S_T, i.e.,

$$y_{T_0,l} = \sum_{m=1}^{M_H} S_{T,m} \exp(-\sum_{k=1}^{K} A_{H,l} \boldsymbol{f}_k), \quad y_{T_0} = \sum_l y_{T_0,l}, \quad (20)$$

where $A_{H,l}$ denotes the path of l-th ray under the high energy scanning geometry, M_H is the total number of sampling at high energy. $\sum_{m=1}^{M_H} S_{T,m} = 1$ and it should be point out that $S_{T,m}$ of the auxiliary spectrum can be equal to $1/M_H$ and the we get pre-computed $\hat{y}_{T_0,l} = \sum_{m=1}^{M_H} S_{T,m} \exp(-A_{H,l} T_0)$. Then, similar to the construction of $\beta^{(n)}, t^{(n)}$, we obtain

$$t_{T_0}(\boldsymbol{f}_1, \boldsymbol{f}_2) = \exp(-\sum_{k=1}^{3} A_{H,l} \boldsymbol{f}_k), \ \beta_{T_0}^{(n)} = \frac{y_{T_0,l}(\boldsymbol{f}_1^{(n)}, \boldsymbol{f}_2^{(n)})}{t_{T_0}(\boldsymbol{f}_1^{(n)}, \boldsymbol{f}_2^{(n)}, \cdots \boldsymbol{f}_K^{(n)})} = \frac{y_{T_0,l}^{(n)}}{t_{T_0}^{(n)}}. \quad (21)$$

Finally, we establish the surrogate function of y_{T_0},

$$\begin{aligned} Ly_{T_0} &= \sum_l y_{T_0,l} - \hat{y}_{T_0,l} \ln y_{T_0,l} \le \sum_l \sum_{m=1}^{M_H} \frac{S_{T,m}}{\beta_{T_0}^{(n)}} (\beta_{T_0}^{(n)} t_{T_0} - \hat{y}_{T_0,l} \ln \beta_{T_0}^{(n)} t_{T_0}) \\ &= \sum_{m=1}^{M_H} S_{T,m} \sum_l \frac{1}{\beta_{T_0}^{(n)}} (\beta_{T_0}^{(n)} t_{T_0} - \hat{y}_{T_0,l} \ln \beta_{T_0}^{(n)} t_{T_0}) \\ &= \sum_{m=1}^{M_H} S_{T,m} \hat{L} y_{T_0}(\boldsymbol{f}_1, \boldsymbol{f}_2, \cdots \boldsymbol{f}_K). \end{aligned} \quad (22)$$

And other derivations are similar to the previous descriptions. Similar as the previous update, Newton's method is applied to obtain the iterative form of the main formula as well while the regularization term is chosen as TV penalty:

$$\begin{aligned} \boldsymbol{f}_k^{(n+1)} &= \boldsymbol{f}_k^{(n)} - \Delta \boldsymbol{f}_k^{(n)} \\ &= \boldsymbol{f}_k^{(n)} - \\ &\frac{\sum_{s,l} A_{s,l}^T \cdot (\frac{\hat{y}_{s,l}}{y_{s,l}^{(n)}} - 1) \sum_{m=1}^{M_k} S_{s,m} \mu_{m,k} t^{(n)} + \sum_l A_{s,l}^T \cdot (\hat{y}_{T_0,l} - y_{T_0,l}^{(n)}) + \lambda \nabla^T \|\nabla \boldsymbol{f}_k\|_1 \Big|_{\boldsymbol{f}_k = \boldsymbol{f}_k^{(n)}}}{\sum_k \sum_{s,l} A_{s,l}^T \cdot A_{s,l} \cdot \sum_{m=1}^{M_k} S_{s,m} \mu_{m,k}^2 t^{(n)} + \sum_l A_{s,l}^T \cdot A_{s,l} \cdot y_{T_0,l}^{(n)} + diag(\nabla^T \nabla) \Big|_{\boldsymbol{f}_k = \boldsymbol{f}_k^{(n)}}}, \\ &(k = 1,2,...,K). \end{aligned} \quad (23)$$

The overall description of the volume conservation constraint based method is summarized in Algorithm 3.

Algorithm 3. VCC-based method

Input: measured projection data $\hat{y}_{s,l}$, parameter $\lambda, n_{\max}$.

Initialization: $\boldsymbol{f}_k^{(0)} (k = 1,2,...,K)$, $n = 0$.

While $n \le n_{\max}$

Update $\boldsymbol{f}_k^{(n)} (k = 1,2,...,K)$ via (19).

End while

Output: $\boldsymbol{f}_k, (k = 1,...,K)$

III. RESULTS

In this section, the performance of the proposed method will be validated through a simulated walnut data[36] and an industrial QRM phantom dataset. The comparison methods are chosen as the three-material EART, the three-material OPMT, the TV-based method listed in Algorithm 1, the DnCNN-based method listed in Algorithm 2, and the VCC-based method listed in Algorithm 3. To further clarify the effectiveness of the proposed algorithms, the root mean square error (RMSE), the peak signal-to-noise ratio (PSNR), and the structural similarity index (SSIM)[37] are employed for quantitative assessment. In addition, to accelerate the algorithms, the ordered subsets (OS) technique[38] is adopted to implement experiments, and the OS number is set to 33 for our proposed methods in the numerical experiments. In the simulation experiments, the regularized penalty parameters λ of the proposed methods are set to 1. And in the real dataset, the corresponding λ of the proposed methods are set to 10^{-2}, 1, and 10^{-3}, respectively. The parameters of comparison methods also modified according to the condition of different datasets. And the total numbers of iterations are set to 3000 and 30 for noisy simulation and real experiments, respectively.

A. SIMULATION EXPERIMENTS

The simulated walnut dataset with size of 512×512 pixels contains three materials, i.e., tissue, bone, and iodine, which is shown in Figure 1(a1)-(a4). And the concentration of iodine contrast agent is 15 mg/mL. The attenuation curves of three materials are shown in Figure 1(b). The distances of source-to-object and source-to-detector are 300.0 mm and 600.0 mm. The three source spectrums for the simulation data are generated by the SpekCalc software[39] at 80 kVp, 110 kVp, and 140 kVp, the distributions are shown in Figure 1(c). Projections of each spectrum are acquired from 363 views uniformly distributed in the 360° range under a fan beam scanning geometry. And the number of detector units is 1024 with size of 0.124 mm. The ray paths of three spectrums are inconsistent to obtain the measured projections in the fast kVp switching scanning. In the experiments, the initial images for all methods are set to zero, and the spectrums used in VCC-based method are the high and low voltages, i.e., 80 kVp and 140 kVp.

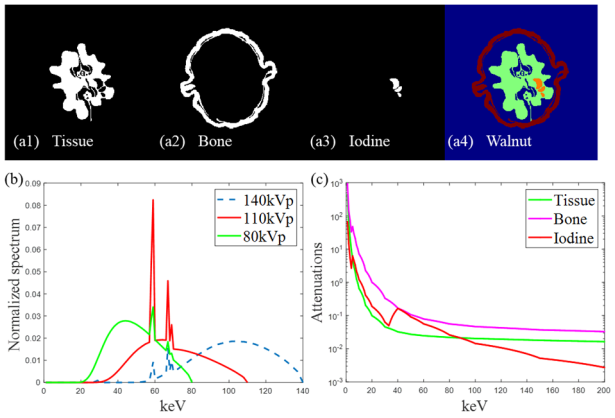

Figure.1 (a) Simulation walnut phantom that consists of (a1) tissue, (a2) bone, and (a3) iodine and (a4) represents the simulated object. (b) Three normalized spectrums used in the simulation experiments. (c) Linear attenuations of different materials.

B. NOISE-FREE DATA VERIFICATION

In this subsection, the ideal noise-free walnut data are first applied to verify the performance of the proposed methods. Figure 2 shows the materials maps reconstructed by the proposed method, where columns (a) to (d) represent the ground truth (Reference), the TV-based method, the DnCNN-based method, and the VCC-based method, respectively. Rows from up to bottom are the distributions of tissue, bone, and iodine materials. According to the results shown in Figure 2, the material maps reconstructed by the proposed methods are close to the given phantom maps in most areas. Since DnCNN is a pre-trained network, it is easy to overfit when the number of iterations is too large. This is also shown by the results reconstructed by DnCNN-based method. For example, it shows some bone structures in the tissue map, as shown by purple arrows in Figure 2 (b1). We further plot the RMSE curves of different materials for the three proposed methods.

As shown in Figure 3(a), the proposed VCC-based method has a faster descent trend compared with the TV-based method and the DnCNN-based method. The reason for this phenomenon is that the former only utilize two spectrums to update, while the latter requires three energies to acquire three material maps. Meanwhile, DnCNN based method has an upward trend with the increase of iteration due to the overfitting. In addition, three different forms of the volume conservation constraint are test.

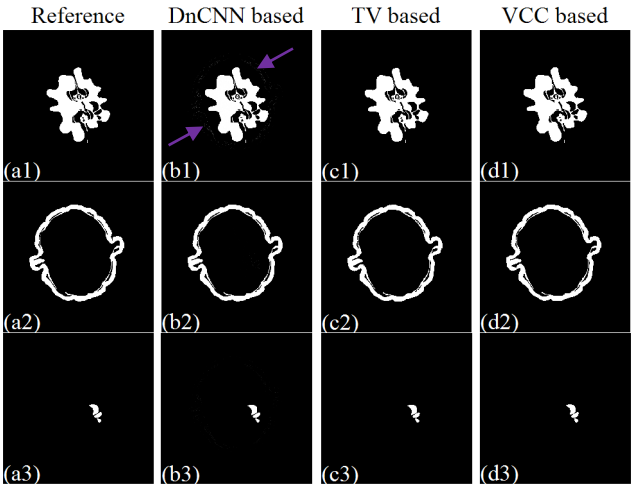

Figure 2. Results of noise-free simulation dataset obtained by the proposed methods. Columns (a) to (d) represent the Reference, the TV-based method, the DnCNN-based method, and the VCC-based method, respectively. Rows from top to bottom indicate three materials: tissue, bone, and iodine, respectively, where the display windows of the first two columns are [0.02 1], [0.01 1], and [0.01 1], respectively.

In Figure 3(b), the high spectrum represents the high energy (140 kVp) used in the simulation experiments. The

equal spectrum means that the normalized spectrum used in VCC-based method is discretized into 140 sampling points, and the intensity of every point is equal. And 2-equal spectrum indicates that we computed two volume conservation constraints in the implementation with two equal spectrums at 140 sampling points and 80 sampling points. The results of RMSEs shows that the high spectrum and equal spectrum have the same positive effect on the algorithm. Their curves overlap in Figure 3(b). And the 2-equal spectrum also declined, and at a faster rate than the other two tested spectrums. The reason for this phenomenon is that the two equality constraints at two spectrums are enforced to accelerate the convergence. From these results, it demonstrates that the introduction of the volume conservation constraint in the VCC-based method plays an important role in multi-material reconstruction and it does not require additional estimation of spectrum. Note that the results of VCC-based method obtained by the usage of two equality constraints.

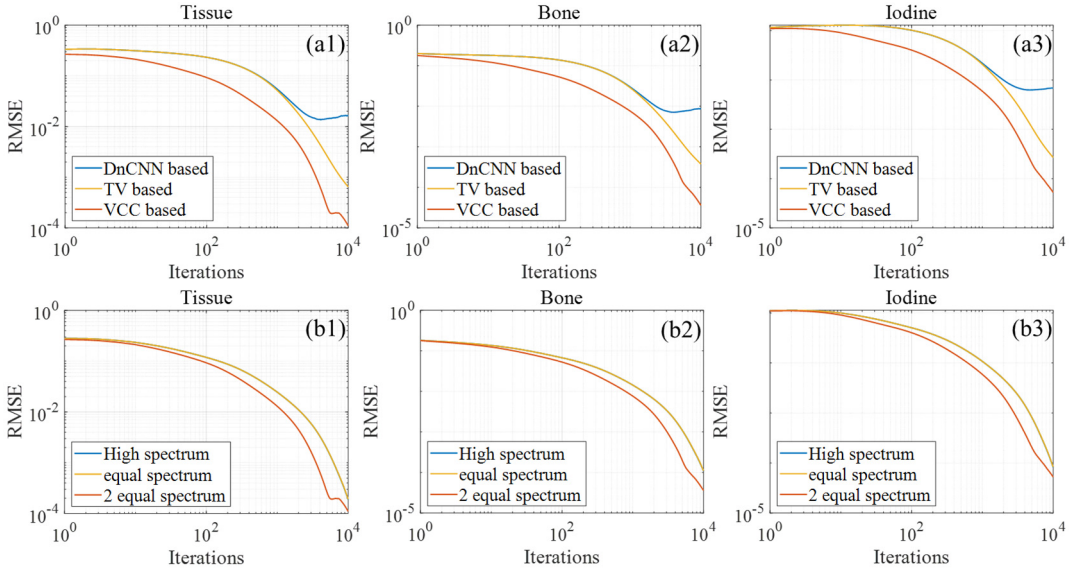

Figure 3. (a) The RMSE curves of the proposed three methods, (b) The verified RMSE curves of different spectrums used in the VCC-based method. Columns from left to right represent tissue, bone, and iodine materials.

C. COMPARISON EXPERIMENTS WITH NOISY DATA

In this subsection, comparison with the state-of-art algorithms will be carried out to further verify the performance of the proposed method. To make the data more realistic, different Poisson noise levels are added to obtained projections to simulate image noises. In this work, Poisson noise is generated and injected into the projections to simulate noisy measurements as

$$P = \frac{I_0^{\,k}}{k!} e^{-I_0}, \boldsymbol{p}_i = P \cdot \exp(-\boldsymbol{p}_0), \qquad (24)$$

where I_0 stands for the number of incident X-ray photons, $\boldsymbol{p}_0, \boldsymbol{p}$ are the measured projection data and the photons of adding noise collected by the detector unit i, respectively. k is the index of detector unit. In this work, we set $I_0 = 1e5$ and $I_0 = 1e7$ to validate the effectiveness of the proposed algorithm.

Figure 4 and Figure 5 show the materials results and virtual monochromatic image at 75 keV reconstructed by different methods at two different noise levels, where the columns (a) to (f) represents the images of Reference, EART, OPMT, TV-based method, DnCNN-based method, and VCC-based method, respectively. Compared with Reference, the results of the EART method is relatively inaccurate, especially in the imaging of tissue, there are still parts of bone in tissue images. The results of OPMT method have a considerable improvement. But at the high noise level, the tissue map of OPMT has obvious noise due to the lack of noise suppression capability, especially in the area marked by purple arrow in Figure 5 (c4). Compared with EART and OPMT methods, the three prior-based methods have the ability of suppressing noise, which have been indicated in the reconstructed material maps. In particular, there are some misclassifications in the tissue and iodine basis materials of DnCNN-based method. The reason is that DnCNN method is derived under the ADMM framework and its decreasing trend is slower than that of Newton method with the same iterations. Furthermore, the last rows of Figure 4 and Figure 5 demonstrate the virtual monochromatic images of different methods. The results show that the proposed methods have the ability of suppressing noise when compared with the EART and OPMT algorithms.

Quantitative evaluations are list in Table 1. Taking the high noise level $I_0 = 1e5$ as an example to illustrate the overall performance of different methods. It can be seen from Table 1 that the averaged PSNRs for three materials of the proposed three algorithms are 32.951 dB, 42.009 dB and 47.173 dB, respectively. And the highest value is obtained by the VCC-based method, which increased PSNRs by

20.924 dB and 18.283 dB compared with those of the EART and OPMT methods, respectively. And the averaged SSIMs for the proposed three algorithms are all over 0.94, where the VCC-based method obtains the highest SSIM index 0.999, while the SSIMs of EART and OPMT are below 0.94. In addition, the highest averaged RMSE among the three proposed algorithms is 0.00592, which reduced RMSEs by 89.65% and 88.79% compared with those of the EART and OPMT methods. The line profiles of different materials, drawn from the pixels along the white dashed line in Fig. 4 (a1) and Fig.5 (a1), are further plotted in Fig.6. It demonstrates that the TV-based method and VCC-based method obtain more accurate structures and details than EART and OPME methods, especially in the areas pointed by the purple arrows.

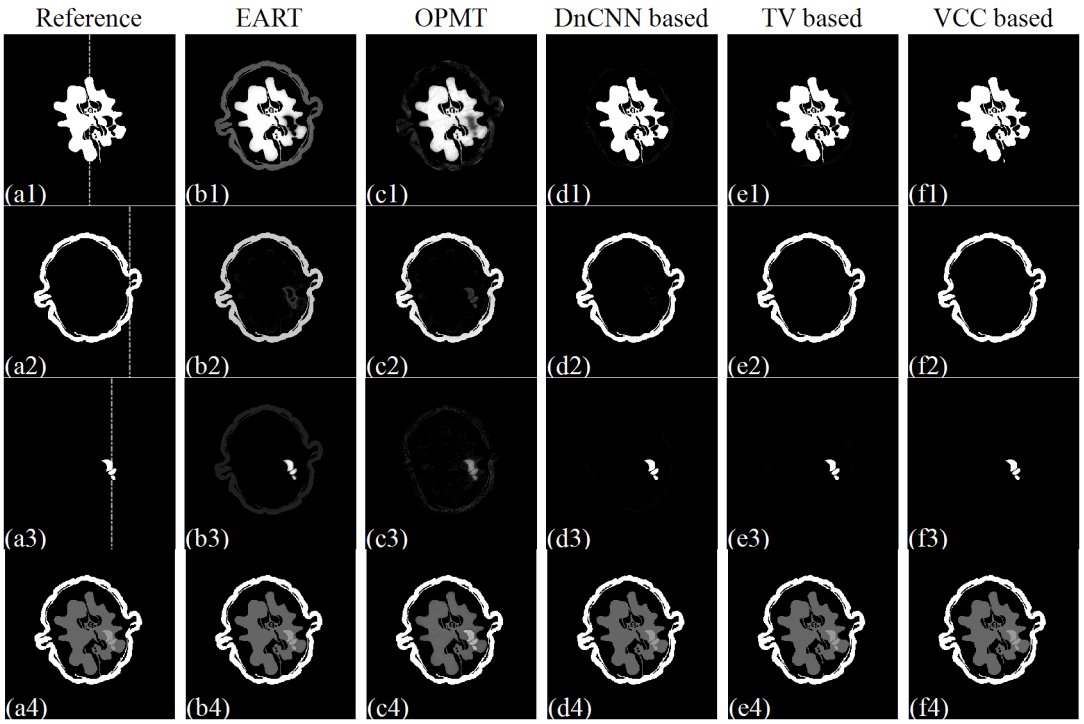

Figure 4. Results of simulation dataset obtained by different methods with noise (I_0 = 1e7). Columns (a) to (f) represent the Reference, EART method, OPMT method, the TV-based method, the DnCNN-based method, and the VCC-based method, respectively. Rows from top to bottom indicate three materials: tissue, bone, iodine, and virtual monochromatic image at 75 keV, respectively, where the display windows of the display windows are [0.02 1], [0.01 1], [0.01 1], and [0.001 0.055], respectively.

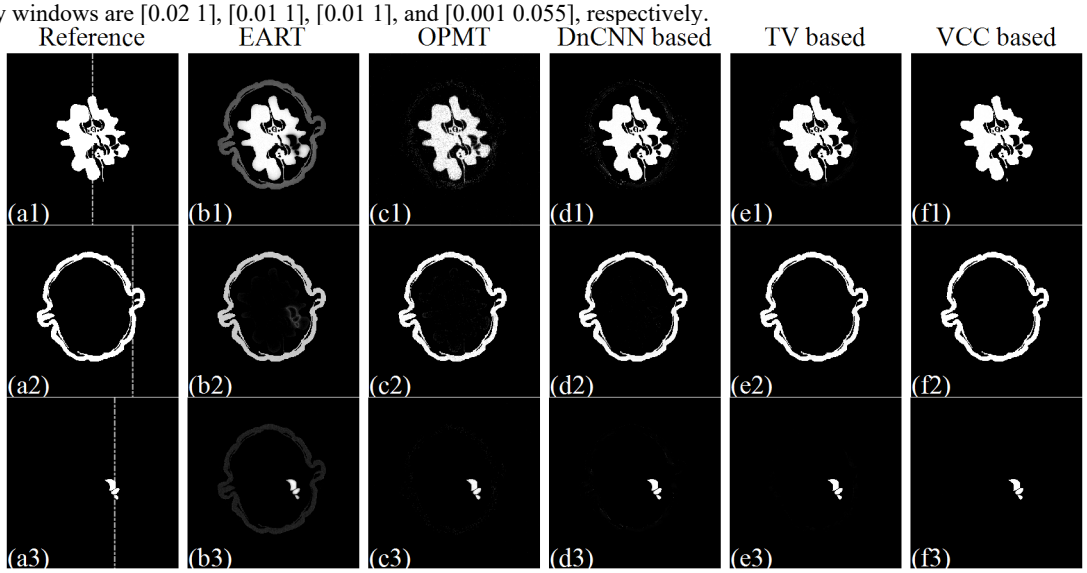

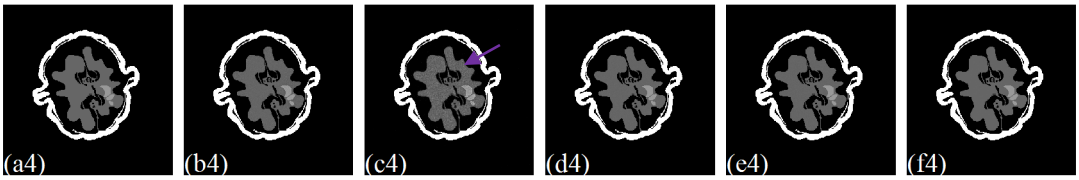

Figure 5. Results of simulation dataset obtained by different methods with noise (I_0 = 1e5). Columns (a) to (f) represent the Reference, EART method, OPMT method, the TV-based method, the DnCNN-based method, and the VCC-based method, respectively. Rows from top to bottom indicate three materials: tissue, bone, iodine, and virtual monochromatic image at 75 keV, respectively, where the display windows of the display windows are [0.02 1], [0.01 1], [0.01 1], and [0.001 0.055], respectively.

Table 1. Quantitative results of different methods.

Algorithm	Materials	Noisy(I_0 = 1e7)			Noisy(I_0 = 1e5)		
		PSNR	SSIM	RMSE	PSNR	SSIM	RMSE
EART	Tissue	19.677	0.882	1.04e-1	19.665	0.866	1.04e-1
	Bone	32.460	0.942	2.38e-2	31.105	0.934	2.78e-2
	Iodine	27.950	0.899	4.00e-2	27.976	0.899	3.99e-2
	Averaged	26.696	0.908	5.59e-2	26.249	0.899	5.72e-2
OPMT	Tissue	22.043	0.855	7.90e-2	18.721	0.817	1.16e-1
	Bone	30.568	0.952	2.96e-2	30.847	0.942	2.87e-2
	Iodine	27.335	0.847	4.30e-2	37.103	0.959	1.40e-2
	Averaged	26.649	0.884	5.05e-2	28.891	0.906	5.28e-2
DnCNN-based	Tissue	35.312	0.943	1.72e-2	27.088	0.901	4.42e-2
	Bone	40.833	0.991	9.09e-3	32.182	0.981	2.46e-2
	Iodine	42.551	0.969	7.45e-3	39.582	0.948	1.05e-2
	Averaged	39.566	0.968	1.12e-2	32.951	0.943	2.64e-2
TV-based	Tissue	41.939	0.967	8.00e-3	31.662	0.932	2.61e-2
	Bone	47.096	0.997	4.42e-3	45.671	0.998	5.21e-3
	Iodine	49.864	0.981	3.21e-3	48.694	0.973	3.68e-3
	Averaged	46.299	0.981	5.21e-3	42.009	0.968	1.17e-2
VCC-based	Tissue	53.669	0.999	2.07e-3	39.026	0.995	1.12e-2
	Bone	58.151	1	1.24e-3	45.837	0.999	5.11e-3
	Iodine	61.447	0.999	8.47e-4	56.656	1	1.47e-3
	Averaged	**57.756**	**0.999**	**1.39e-3**	**47.173**	**0.998**	**5.92e-3**

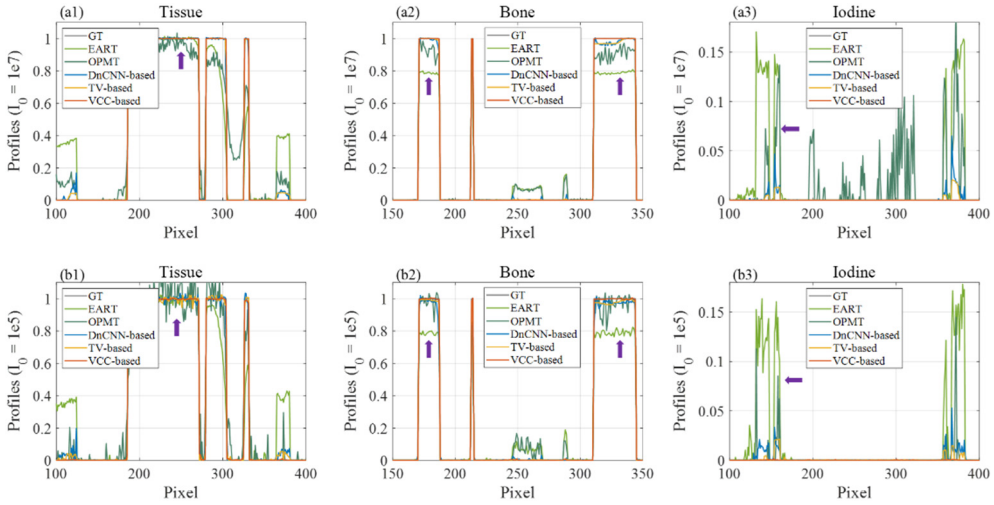

Figure 6. Profiles of different methods at different noise levels

D. REAL QRM DATA EXPERIMENT

In this section, the performance of the proposed methods are investigated by an industrial QRM phantom, which consists of five different materials including cortical mandible bone, spongious bone, muscle, CT water, and adipose. The diameters of the phantom and each cylinder are 100.0 mm and 20.0 mm, respectively. It should be pointed out that two different densities of bone are considered to bone basis

material, CT water and adipose are seemed as water basis material with impurities, which is shown in Figure 7.

The QRM phantom data is obtained using an industrial CT system in our laboratory under a cone beam system, which mainly composes of an X-ray rotary stage with an object holder and flat panel detector (4030E, Varian, USA). The QRM are scanned repeatedly at tube voltages 60, 80, and 100 kVp along a circular line and the tube current is set to 220 μA for every scanning. The central slice of each two-dimensional projection is extracted and down-sampled as 512 detector bins for the materials reconstruction in this experiment. The source to object and detector distances are 245.0 mm and 808.0 mm, respectively. The projections corresponding to the three X-ray scanning are obtained in an alternating mode, i.e., the paths of ray are geometrically inconsistent. A total 720 projection views are collected in 360° range for each scanning.

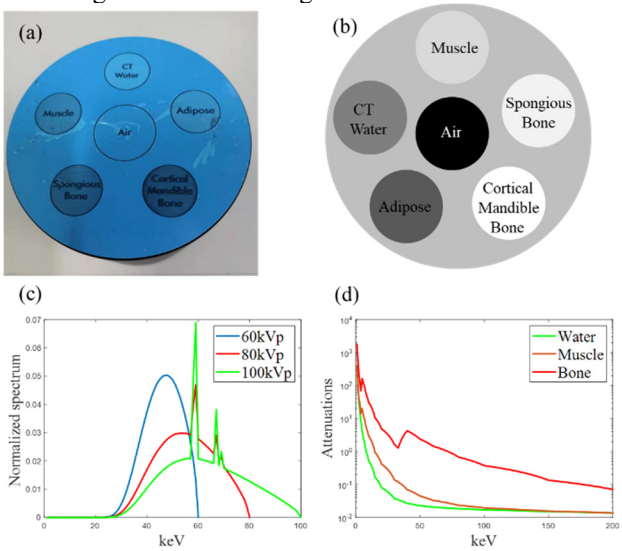

Figure 7. QRM phantom consists of five materials: cortical mandible bone, spongious bone, muscle, CT water, and adipose, where (a) represents the real QRM object; (b) represents the schematic diagram of five materials. And (c) plots the estimated three spectrums, (d) draws the linear attenuations of three basis materials.

The pixels of reconstructed image are 512×512 with each size of 0.252×0.252 mm^2. And the spectrums are estimated by the expectation-maximization (EM) method[40], which are shown in Figure 7 (c). The linear attenuations of three basis materials used in our experiments are drawn in Figure 7 (d). Some regions of interest (ROIs) (denoted in red dotted squares Figure 8) are chosen to make quantitative evaluation of the mean value of attenuation coefficients and standard deviation (STD), which is calculated as follows

$$STD = \sqrt{\frac{1}{N_{roi}} \sum_{r=1}^{N_{roi}} (x_r - \bar{x})^2}, \qquad (25)$$

where x_r denote the value of r-th pixel. $\bar{x}$ is the pre-computed mean value of all N_{roi} image pixels of the selected ROI. And Some ROIs (denoted in yellow dotted squares in Figure 9) are magnified to assess the noise suppression across the different algorithms. Furthermore, the projection views are downsampled to 360 to assess the performance of the proposed methods.

Figure 8 shows the reconstructed results of all methods, where columns from (a) to (e) represent EART method, OPMT method, DnCNN based method, TV-based method, and VCC-based method, respectively. Rows from up to bottom represent the three materials, i.e., water, muscle, and bone. Note that the proposed VCC-based method chooses the spectrums generated by tube voltages 60 kVp and 100 kVp. As shown in Figure 8, all the five methods can obtain the maps of three materials. However, due to the lack of denoising ability, some noises appear in the results reconstructed by EART and OPMT methods, which can be obviously seen from the reconstruction results of water basis material in Figure 8 (a1) and (b1), marked by purple arrows. And there are some other structures of muscle and water in the bone maps, as denoted by purple arrows in Figure 8 (a3) and (b3). The remaining three methods are all the methods proposed in this paper, and they have the advantages in noise suppression to a certain extent. To further illustrate the effectiveness of one-step method in eliminating beam-hardening, virtual monochromatic images are further shown in Figure 9. Figure 9 displays the results of virtual monochromatic images between the five iterative methods at single energy 70, and 110 keV, respectively. The results of EART and OPMT show that the reconstructed images is not smooth and uneven due to the existence of noise, especially in the region marked by purple arrows. Compared with the results reconstructed by EART and OPMT, the other three iterative one-step methods has abilities of suppressing noises, as can be observed from the ROIs in Figure 9. The downsampled results of 360 projection views, shown in Figure 10 and 11, also have the similar opinions.

Table 2 further list the quantitative evaluations of different methods under 720 projection views, where the mean value is measured to assess the accuracy of the results, while the STD value evaluates the noise suppression ability of different methods. The STD values of the proposed methods also demonstrate that the proposed methods are superior in suppressing noises. The reference values of three ROIs are computed according to the threshold segmentation results of filtered backprojection algorithm reconstructions. From the Table 2, the proposed methods have similar mean values in ROI 3 with other methods, indicating the accuracy of reconstruction results, while the STD values show the advantages of the proposed methods in ROI 1 and ROI 3 compared with other methods.

This article has been accepted for publication in IEEE Access. This is the author's version which has not been fully edited and content may change prior to final publication. Citation information: DOI 10.1109/ACCESS.2023.3261661

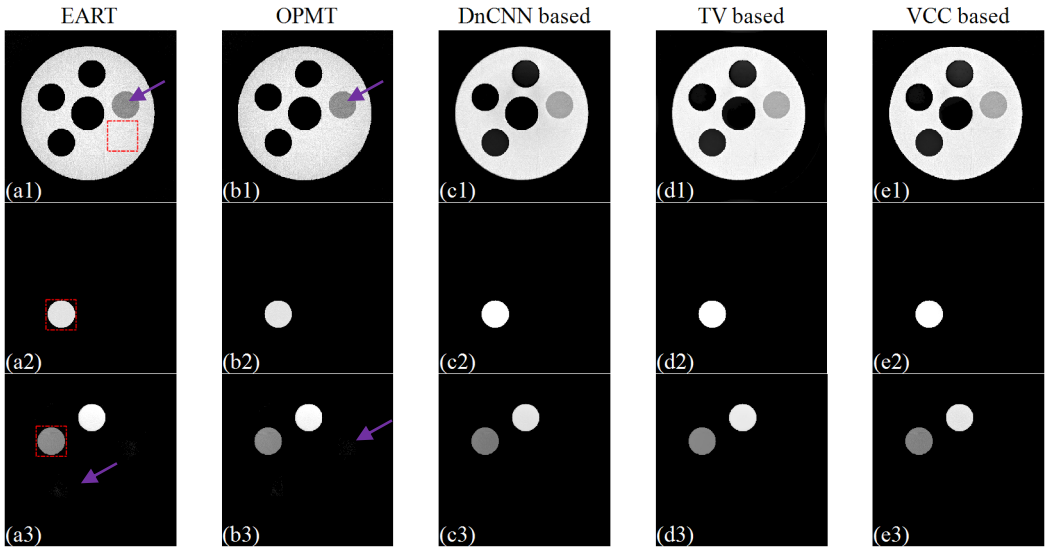

Figure 8. Reconstructed three material images of different methods under 720 projection views. Columns from (a) to (e) represents the EART method, OPMT method, DnCNN based method, TV-based method, and VCC-based method, respectively. Rows from up to bottom represent water, muscle, and bone. And the corresponding display windows are [0 1.1], [0 0.5], and [0 0.04].

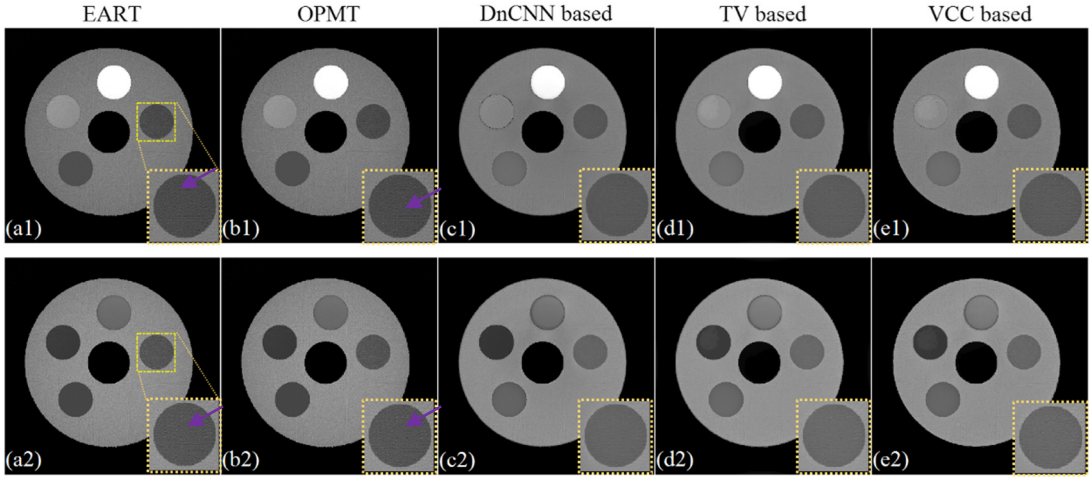

Figure 9. Virtual monochromatic images and the corresponding enlarged areas of different methods under 720 projection views. The first row represents the images at 70 keV and the second row represents the images at 110 keV. And the display windows are [0 0.04] and [0 0.03].

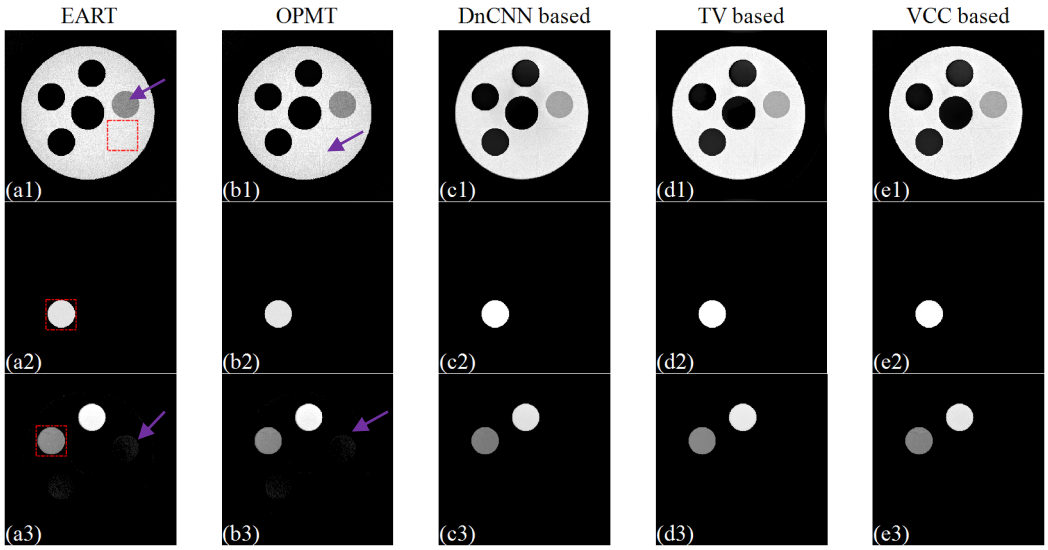

Figure 10. Reconstructed three material images of different methods under 360 projection views. Columns from (a) to (e) represents the EART method, OPMT method, DnCNN based method, TV-based method, and VCC-based method, respectively. Rows from up to bottom represent water, muscle, and bone. And the corresponding display windows are [0 1.1], [0 0.5], and [0 0.04].

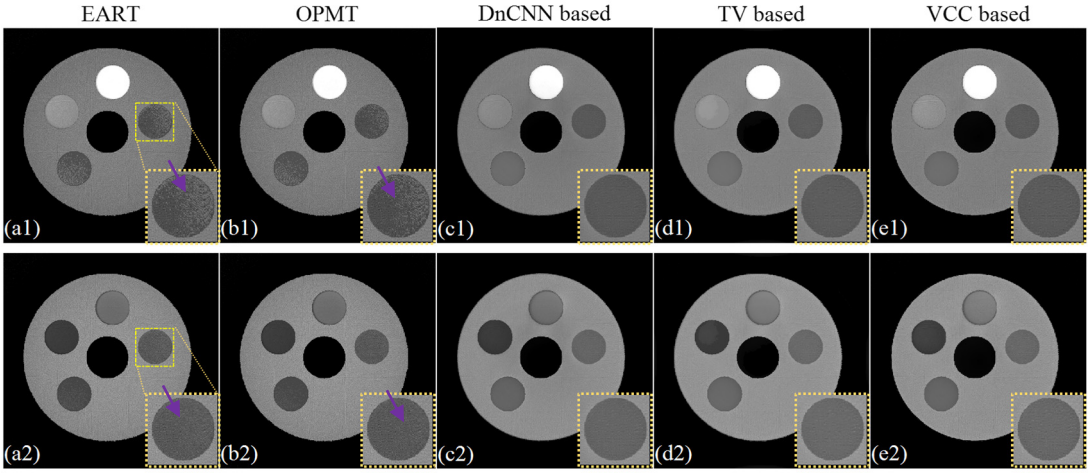

Figure 11. Virtual monochromatic images and the corresponding enlarged areas of different methods under 360 projection views. The first row represents the images at 70 keV and the second row represents the images at 110 keV. And the display windows are [0 0.04] and [0 0.03].

Table 2. The comparison of mean values and standard deviations for different methods

	ROI	Reference	EART	OPMT	DnCNN-based	TV-based	VCC-based
720 views	1	1.005±0.063	1.005±0.063	1.005±0.063	0.9901±0.033	1.036±0.025	1.019±0.014
	2	0.284±0.211	0.282±0.214	0.283±0.214	0.324±0.246	0.323±0.245	0.317±0.240
	3	0.014±0.010	0.014±0.010	0.014±0.010	0.012±0.009	0.013±0.010	0.013±0.010

IV. DISCUSSIONS

In this paper, we consider the multi-material reconstruction problem in the case of each energy spectrum has inconsistent scanning path. Note that the ill-condition of the multi-material reconstruction problem will be intensified with the increase of the number of materials, especially under inconsistent scanning geometry. The projection-domain methods don't work for the inconsistent path. It is more difficult to obtain accurate distributions of basis materials based on image-domain approaches when basis materials have similar attenuations. Aiming at this situation, a statistical multi-material based one-step reconstruction model is considered to describe a more realistic distributions of photons. The model is firstly simplified by incorporating the statistical upper bound. Then, fidelity data term further combines sparsity-based TV regularization term and deep prior-based regularization term to integrate the noise suppression in each iteration of material reconstruction when the number of energies matches the number of material. In addition, when the number of energies and number of materials do not match, a new volume conservation constraint is developed to improve the ill-condition of the inverse problem. Moreover, several numerical experiments are carried out to verify the effectiveness of the proposed methods. The results show that the practical performance is consistent with the original design, and it can obtain a relatively stable solution while suppressing noise. The monochromatic imaging results, as shown in Figure.9, further indicates the proposed method has the ability to suppress noise.

Although the proposed algorithms show that it is useful for the multi-material reconstruction, model-driven methods based on certain assumptions cannot fully express the physical mechanism for the realistic application of CT imaging, for example, the response of detector units are different for certain spectrum, and noise in the measured projections is easily multiple amplified in the reconstructed process of basis materials. The disturbance of noise is a huge instability factor for the convergence of the algorithm. As a result, data-driven methods for materials reconstruction have also been developed, such as Zhang *et al.*[41] proposed a butterfly network to realize material decomposition based on image-domain under dual-energy. Fang et al. applied the unsupervised denoising method called Noise2Noise[42] as the prior knowledge to estimate the material maps directly from the raw projection data[43]. And other researcheres also find the deep learning based method has certain advantages in medical image analysis[44-47]. These methods also encourage us to combine model-driven and data-driven methods to achieve accurate decomposition of materials by eliminating the influence of beam-hardening artifacts while suppressing noise in the future.

V. CONCLUSIONS

For the inconsistent material-specific reconstruction, this paper applies a statistical model with different prior to

establish material reconstruction model. First, the gradient sparsity-based and deep prior-based regularization terms are incorporated into the optimization problem to update the material maps when the numbers of materials and energies are consistent. Then, the volume conservation constraint is further added to improve the convergence rate when the numbers of materials and energies are not consistent. Furthermore, the ordered subsets are applied to accelerate the proposed algorithms. The simulation and real data experiments verify the effectiveness of the proposed methods in basis material reconstruction, and also the capabilities in suppressing noise.

CONFLICT OF INTEREST

The authors have no conflicts of interest to declare.

ACKNOWLEDGMENT

The authors would like to thank the editors and the anonymous reviewers whose insightful comments have helped to improve the quality of this paper considerably.

REFERENCES

[1] S. C. Brandelik, S. Skornitzke, T. Mokry, S. Sauer, W. Stiller, J. Nattenmüller, H. U. Kauczor, T. F. Weber, and T. D. Do, "Quantitative and qualitative assessment of plasma cell dyscrasias in dual-layer spectral CT," *European Radiology,* vol. 31, no. 10, pp. 7664-7673, 2021.

[2] W. Wu, D. Hu, K. An, S. Wang, and F. Luo, "A high-quality photon-counting CT technique based on weight adaptive total-variation and image-spectral tensor factorization for small animals imaging," *IEEE Transactions on Instrumentation and Measurement,* vol. 70, pp. 1-14, 2020.

[3] S. Wang, W. Wu, J. Feng, F. Liu, and H. Yu, "Low-dose spectral CT reconstruction based on image-gradient L0-norm and adaptive spectral PICCS," *Physics in Medicine & Biology,* vol. 65, no. 24, pp. 245005, 2020.

[4] B. Daoud, J. Cazejust, S. Tavolaro, S. Durand, R. Pommier, A. Hamrouni, and G. Bornet, "Could Spectral CT Have a Potential Benefit in Coronavirus Disease (COVID-19)?," *American Journal of Roentgenology,* vol. 216, no. 2, pp. 349-354, 2020.

[5] A. Agostini, C. Floridi, A. Borgheresi, M. Badaloni, P. Esposto Pirani, F. Terilli, L. Ottaviani, and A. Giovagnoni, "Proposal of a low-dose, long-pitch, dual-source chest CT protocol on third-generation dual-source CT using a tin filter for spectral shaping at 100 kVp for CoronaVirus Disease 2019 (COVID-19) patients: a feasibility study," *La radiologia medica,* vol. 125, no. 4, pp. 365-373, 2020.

[6] K. Taguchi, and J. S. Iwanczyk, "Vision 20/20: Single photon counting x-ray detectors in medical imaging," *Medical Physics,* vol. 40, no. 10, pp. 100901, 2013.

[7] N. G. Anderson, A. P. Butler, N. J. A. Scott, N. J. Cook, J. S. Butzer, N. Schleich, M. Firsching, R. Grasset, N. de Ruiter, M. Campbell, and P. H. Butler, "Spectroscopic (multi-energy) CT distinguishes iodine and barium contrast material in MICE," *European Radiology,* vol. 20, no. 9, pp. 2126-2134, 2010.

[8] J. Noh, J. A. Fessler, and P. E. Kinahan, "Statistical Sinogram Restoration in Dual-Energy CT for PET Attenuation Correction," *IEEE Transactions on Medical Imaging,* vol. 28, no. 11, pp. 1688-1702, 2009.

[9] R. E. Alvarez, "Estimator for photon counting energy selective x-ray imaging with multibin pulse height analysis," *Medical Physics,* vol. 38, no. 5, pp. 2324-2334, 2011.

[10] T. Niu, X. Dong, M. Petrongolo, and L. Zhu, "Iterative image-domain decomposition for dual-energy CT," *Medical Physics,* vol. 41, no. 4, pp. 041901, 2014.

[11] C. Maaß, M. Baer, and M. Kachelrieß, "Image-based dual energy CT using optimized precorrection functions: A practical new approach of material decomposition in image domain," *Medical Physics,* vol. 36, no. 8, pp. 3818-3829, 2009.

[12] Q. Ding, T. Niu, X. Zhang, and Y. Long, "Image-domain multimaterial decomposition for dual-energy CT based on prior information of material images," *Medical Physics,* vol. 45, no. 8, pp. 3614-3626, 2018.

[13] R. E. Alvarez, and A. Macovski, "Energy-selective reconstructions in X-ray computerised tomography," *Physics in Medicine and Biology,* vol. 21, no. 5, pp. 733-744, 1976.

[14] A. Sawatzky, Q. Xu, C. O. Schirra, and M. A. Anastasio, "Proximal ADMM for Multi-Channel Image Reconstruction in Spectral X-ray CT," *IEEE Transactions on Medical Imaging,* vol. 33, no. 8, pp. 1657-1668, 2014.

[15] J. P. Schlomka, E. Roessl, R. Dorscheid, S. Dill, G. Martens, T. Istel, C. Bäumer, C. Herrmann, R. Steadman, G. Zeitler, A. Livne, and R. Proksa, "Experimental feasibility of multi-energy photon-counting K-edge imaging in pre-clinical computed tomography," *Physics in Medicine and Biology,* vol. 53, no. 15, pp. 4031-4047, 2008.

[16] Z. Yu, and D. S. Michael, "Analysis of fast kV-switching in dual energy CT using a pre-reconstruction decomposition technique."

[17] S. Faby, S. Kuchenbecker, S. Sawall, D. Simons, H.-P. Schlemmer, M. Lell, and M. Kachelrieß, "Performance of today's dual energy CT and future multi energy CT in virtual non-contrast imaging and in iodine quantification: A simulation study," *Medical Physics,* vol. 42, no. 7, pp. 4349-4366, 2015.

[18] Y. Zhao, X. Zhao, and P. Zhang, "An Extended Algebraic Reconstruction Technique (E-ART) for Dual Spectral CT," *IEEE Transactions on Medical Imaging,* vol. 34, no. 3, pp. 761-768, 2015.

[19] J. Hu, X. Zhao, and F. Wang, "An extended simultaneous algebraic reconstruction technique (E-SART) for X-ray dual spectral computed tomography," *Scanning,* vol. 38, no. 6, pp. 599-611, 2016.

[20] W. Zhang, S. Zhao, H. Pan, Y. Zhao, and X. Zhao, "An iterative reconstruction method based on monochromatic images for dual energy CT," *Medical Physics,* vol. 48, no. 10, pp. 6437-6452, 2021.

[21] S. Zhao, H. Pan, W. Zhang, D. Xia, and X. Zhao, "An oblique projection modification technique (OPMT) for fast multispectral CT reconstruction," *Physics in Medicine & Biology,* vol. 66, no. 6, pp. 065003, 2021.

[22] X. Qiong, M. Xuanqin, T. Shaojie, H. Wei, Z. Yizhai, and L. Tao, "Implementation of penalized-likelihood statistical reconstruction for polychromatic dual-energy CT."

[23] Y. Long, and J. A. Fessler, "Multi-Material Decomposition Using Statistical Image Reconstruction for Spectral CT," *IEEE Transactions on Medical Imaging,* vol. 33, no. 8, pp. 1614-1626, 2014.

[24] T. Weidinger, T. M. Buzug, T. Flohr, S. Kappler, and K. Stierstorfer, "Polychromatic Iterative Statistical Material Image Reconstruction for Photon-Counting Computed Tomography," *International Journal of Biomedical Imaging,* vol. 2016, pp. 5871604, 2016.

[25] K. Mechlem, S. Ehn, T. Sellerer, E. Braig, D. Münzel, F. Pfeiffer, and P. B. Noël, "Joint Statistical Iterative Material Image Reconstruction for Spectral Computed Tomography Using a Semi-Empirical Forward Model," *IEEE Transactions on Medical Imaging,* vol. 37, no. 1, pp. 68-80, 2018.

[26] R. Foygel Barber, E. Y. Sidky, T. Gilat Schmidt, and X. Pan, "An algorithm for constrained one-step inversion of spectral CT data," *Physics in Medicine and Biology,* vol. 61, no. 10, pp. 3784-3818, 2016.

[27] R. F. B. a. E. Y. Sidky, "Convergence for nonconvex ADMM, with applications to CT imaging," 2021.

[28] T. G. Schmidt, B. A. Sammut, R. F. Barber, X. Pan, and E. Y. Sidky, "Addressing CT metal artifacts using photon-counting detectors and one-step spectral CT image reconstruction," *Medical Physics,* vol. 49, no. 5, pp. 3021-3040, 2022.

[29] C. Cai, T. Rodet, S. Legoupil, and A. Mohammad-Djafari, "A full-spectral Bayesian reconstruction approach based on the material decomposition model applied in dual-energy computed tomography," *Medical Physics,* vol. 40, no. 11, pp. 111916, 2013.

[30] Q. Xu, A. Sawatzky, M. A. Anastasio, and C. O. Schirra, "Sparsity-regularized image reconstruction of decomposed K-edge data in spectral CT," *Physics in Medicine and Biology,* vol. 59, no. 10, pp. N65-N79, 2014.

[31] B. Chen, Z. Zhang, E. Y. Sidky, D. Xia, and X. Pan, "Image reconstruction and scan configurations enabled by optimization-based algorithms in multispectral CT," *Physics in Medicine & Biology,* vol. 62, no. 22, pp. 8763-8793, 2017.

[32] B. Chen, Z. Zhang, D. Xia, E. Y. Sidky, and X. Pan, "Non-convex primal-dual algorithm for image reconstruction in spectral CT," *Computerized Medical Imaging and Graphics,* vol. 87, pp. 101821, 2021.

[33] W. Zhang, A. Cai, Z. Zheng, L. Wang, N. Liang, L. Li, B. Yan, and G. Hu, "A Direct Material Reconstruction Method for DECT Based on Total Variation and BM3D Frame," *IEEE Access,* vol. 7, pp. 138579-138592, 2019.

[34] K. Zhang, W. Zuo, Y. Chen, D. Meng, and L. Zhang, "Beyond a gaussian denoiser: Residual learning of deep cnn for image denoising," *IEEE transactions on image processing,* vol. 26, no. 7, pp. 3142-3155, 2017.

[35] S. V. Venkatakrishnan, C. A. Bouman, and B. Wohlberg, "Plug-and-play priors for model based reconstruction." pp. 945-948.

[36] J. S. Jørgensen, and E. Y. Sidky, "How little data is enough? Phase-diagram analysis of sparsity-regularized X-ray computed tomography," *Philosophical Transactions of the Royal Society A: Mathematical, Physical and Engineering Sciences,* vol. 373, no. 2043, pp. 20140387, 2015.

[37] W. Zhou, A. C. Bovik, H. R. Sheikh, and E. P. Simoncelli, "Image quality assessment: from error visibility to structural similarity," *IEEE Transactions on Image Processing,* vol. 13, no. 4, pp. 600-612, 2004.

[38] H. Erdogan, and J. A. Fessler, "Ordered subsets algorithms for transmission tomography," *Physics in Medicine and Biology,* vol. 44, no. 11, pp. 2835-2851, 1999.

[39] G. Poludniowski, G. Landry, F. DeBlois, P. M. Evans, and F. Verhaegen, "SpekCalc: a program to calculate photon spectra from tungsten anode x-ray tubes," *Physics in Medicine and Biology,* vol. 54, no. 19, pp. N433-8, 2009.

[40] E. Y. Sidky, L. Yu, X. Pan, Y. Zou, and M. Vannier, "A robust method of x-ray source spectrum estimation from transmission measurements: Demonstrated on computer simulated, scatter-free transmission data," *Journal of applied physics,* vol. 97, no. 12, pp. 124701, 2005.

[41] W. Zhang, H. Zhang, L. Wang, X. Wang, X. Hu, A. Cai, L. Li, T. Niu, and B. Yan, "Image domain dual

material decomposition for dual-energy CT using butterfly network," *Medical Physics,* vol. 46, no. 5, pp. 2037-2051, 2019.

[42] J. Lehtinen, J. Munkberg, J. Hasselgren, S. Laine, T. Karras, M. Aittala, and T. Aila, "Noise2Noise: Learning Image Restoration without Clean Data," *arXiv,* vol. 2018, pp. 1803.04189, 2018.

[43] W. Fang, D. Wu, K. Kim, M. K. Kalra, R. Singh, L. Li, and Q. Li, "Iterative material decomposition for spectral CT using self-supervised Noise2Noise prior," *Physics in Medicine and Biology,* vol. 66, no. 15, pp. 155013, 2021.

[44] S. Wang, H. Yu, Y. Xi, C. Gong, W. Wu, and F. Liu, "Spectral-image decomposition with energy-fusion sensing for spectral CT reconstruction," *IEEE Transactions on Instrumentation and Measurement,* vol. 70, pp. 1-11, 2021.

[45] T. Zhang, H. Yu, Y. Xi, S. Wang, and F. Liu, "Spectral CT Image-domain Material Decomposition via Sparsity Residual Prior and Dictionary Learning," *IEEE Transactions on Instrumentation and Measurement*, 2022.

[46] W. Wu, X. Guo, Y. Chen, S. Wang, and J. Chen, "Deep Embedding-Attention-Refinement for Sparse-view CT Reconstruction," *IEEE Transactions on Instrumentation and Measurement*, 2022.

[47] S. Wang, W. Wu, A. Cai, Y. Xu, V. Vardhanabhuti, F. Liu, H. Yu. "Image-spectral decomposition extended-learning assisted by sparsity for multi-energy computed tomography reconstruction," Quantitative Imaging in Medcine and Surgery 2022.

Xiaohuan Yu received the M.S. degree from the Zhengzhou University, and she is currently pursuing the Ph.D. degree from the College of Information Engineering, Information Engineering University, Zhengzhou, China. Her research interests including theory and application of imaging, especially on intelligent algorithms for inverse problems, image processing, spectral computed tomography, and its applications on biomedical and industrial fields.

Ailong Cai received the B.S., M.S., and Ph.D. degrees from the College of Information Engineering, Information Engineering University, Zhengzhou, China, in 2011, 2014, and 2018, respectively. He is currently an associated professor with the College Information Engineering and the Key Laboratory of Imaging and Intelligent Processing of Henan Province. His research interests including theory and application of imaging, especially on intelligent algorithms for inverse problems, image processing, spectral computed tomography, and its applications on biomedical and industrial fields.

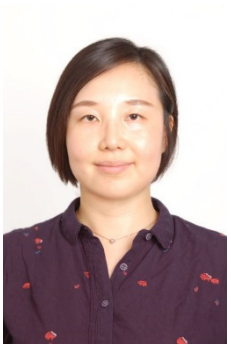

Ningning Liang was born in Tianjin, China, in 1982. She received the B.S., M.S., and Ph.D. degrees from the Information Engineering University, Zhengzhou, China, in 2004, 2009, and 2015, respectively. She is currently an associated professor with the Information Engineering University and the deputy director of the Key Laboratory of Imaging and Intelligent Processing of Henan Province. Her research interests include X-ray CT system design and intelligent image processing.

Shaoyu Wang was born in Nanyang, Henan, China, in 1992. He received the M.S. and Ph.D. degree from Chongqing University, Chongqing, in 2018 and 2021. From 2019 to 2020, he was a joint-training Ph.D. Candidate with the University of Massachusetts Lowell. He is currently a lecturer with the College Information Engineering. His research interests include X-ray system design, image reconstruction, and material decomposition. He also achieved the Chinese Scholarship Council Scholarship, in 2019.

Lei Li received the B.S., M.S., and Ph.D. degrees from the College of Information Engineering, Information Engineering University, Zhengzhou, China, in 2003, 2006, and 2016, respectively. He is currently an associated professor of the College of Information Engineering and the Key Laboratory of Imaging and Intelligent Processing of Henan Province. His research interests including theory, technology and application of imaging, especially on X-ray system design, spectral computed tomography, and its applications on biomedical and industrial fields.

Bin Yan graduated from the Chinese Academy of Sciences in 2005 with a physics Ph.D. degree. He is currently a professor with the College Information Engineering, Information Engineering University. His research interests including theory and application of computed tomography imaging, computer vision, and brain computer interaction.